Real-space imaging of magnetization reversal in deformed kagome artificial spin ices

Dong Shi,[1,2] Haoran Chen,[2] Jia Xu,[2] Shilei Zhang,[1,*] and Yizheng Wu[2,3,4,†]

[1]*School of Physical Science and Technology, Shanghai Tech University, Shanghai 200031, People's Republic of China*

[2]*Department of Physics, State Key Laboratory of Surface Physics, Fudan University, Shanghai 200433, People's Republic of China*

[3]*Shanghai Research Center for Quantum Sciences, Shanghai 201315, People's Republic of China*

[4]*Shanghai Key Laboratory of Metasurfaces for Light Manipulation, Fudan University, Shanghai 200433, People's Republic of China*

(Received 23 September 2023; revised 11 December 2023; accepted 17 January 2024; published 2 February 2024)

The structure symmetry in artificial spin ice systems plays important roles in the magnetization reversal process when subjected to an external magnetic field. We investigated the magnetization reversal processes with different field orientations in the deformed kagome spin ices with threefold symmetry broken using high-resolution Kerr microscopy. Distinct magnetization reversal processes were observed in the deformed kagome system when compared to those found in standard kagome structures. In addition to the previously documented Dirac-string-like and system-size avalanche-type reversals, we identified two unusual reversal behaviors: the armchairlike avalanche and the discrete magnetization reversal within a single bar. These behaviors can be elucidated through the modified energy hierarchy present in the deformed kagome spin ices. Furthermore, we observed that the magnetization reversal behaviors in deformed kagome ice can be manipulated by selecting different initial spin states. These findings contribute to a deeper comprehension of nonequilibrium critical point phenomena in artificial spin ice systems.

DOI: 10.1103/PhysRevB.109.064402

I. INTRODUCTION

Artificial spin ice comprises a two-dimensional (2D) array of nanoscale magnetic elements. It has garnered significant attention due to its ability to emulate the physics of real spin ice in real space [1–14]. Specifically, artificial spin ice systems, like their real counterparts, must adhere to the ice rule to minimize system energy [1,2,15]. In connected spin ice networks, the primary focus lies in understanding the dynamics of domain walls when subjected to an external field [16–27]. This is particularly appealing because domain walls can transport magnetic charges, offering opportunities for controlling magnetic charge propagation, which holds implications for high-density memory storage. The delocalization of domain walls or magnetic charges along specific paths within the spin ice network is a process heavily influenced by the ice rule [28]. Within kagome spin ices, where the ice rule constraint is in effect, magnetization reversal exhibits intriguing collective behaviors, including the formation of "Dirac strings" [17,29,30] and the selective pathways for magnetic charge movement [18–21].

Dynamic behaviors within kagome spin ices were captured in both real space and real-time using high-resolution Kerr microscopy [28], enabling a detailed examination of the magnetization reversal process in real space. Two distinct types of magnetization reversal were identified: one-dimensional Dirac-string-like reversal and two-dimensional system-size avalanches, which also exhibit strong dependence on the angle of the external magnetic field, which possesses a sixfold symmetry. These behaviors align with the principles of the ice rule within the kagome spin ice, involving energy minimization under the constraints akin to those in disconnected kagome ice. Studies have shown that the ice rule in disconnected artificial spin ice systems is sensitive to local structural modifications [12–14]. Such modifications can break geometric symmetry and lift system degeneracy. Consequently, altering the energy hierarchy grants access to previously unreachable ground states and other exotic physical properties [12–14]. Therefore, modifying the structure of standard kagome spin ices, specifically by disrupting their threefold rotational symmetry, leads to the degeneration of the kagome system's ground energy state. This degeneracy significantly influences the dynamic behaviors of magnetization reversal within the deformed kagome spin ices.

In this study, we introduced an asymmetrical structure into the connected kagome spin ice pattern through structural deformation, as illustrated in Figs. 1(a)–1(c). In the standard kagome ice lattice, the angle between sublattice branches is fixed at 120°. However, when subjected to compression along different directions, this angle can either increase or decrease from 120°, resulting in two distinct structural types. The original sixfold degenerate low-energy state divides into two groups of energy levels. We employed high-resolution Kerr microscopy to capture detailed magnetization reversal behaviors in real space during the field sweeping process. Our results confirm that the breaking of structural symmetry leads to significant changes in the pathway of magnetic charge propagation, resulting in various unique avalanche behaviors. In addition to the Dirac-string-like reversal and system-size avalanche-type reversal observed in the standard kagome spin ice system, we observed two unusual reversal behaviors: the armchairlike avalanche and the discrete magnetization reversal within a single bar. Furthermore, we found that the Dirac-string-like reversal behaviors in the deformed kagome

*shilei.zhang@shanghaitech.edu.cn

†Author to whom correspondence should be addressed: wuyizheng@fudan.edu.cn

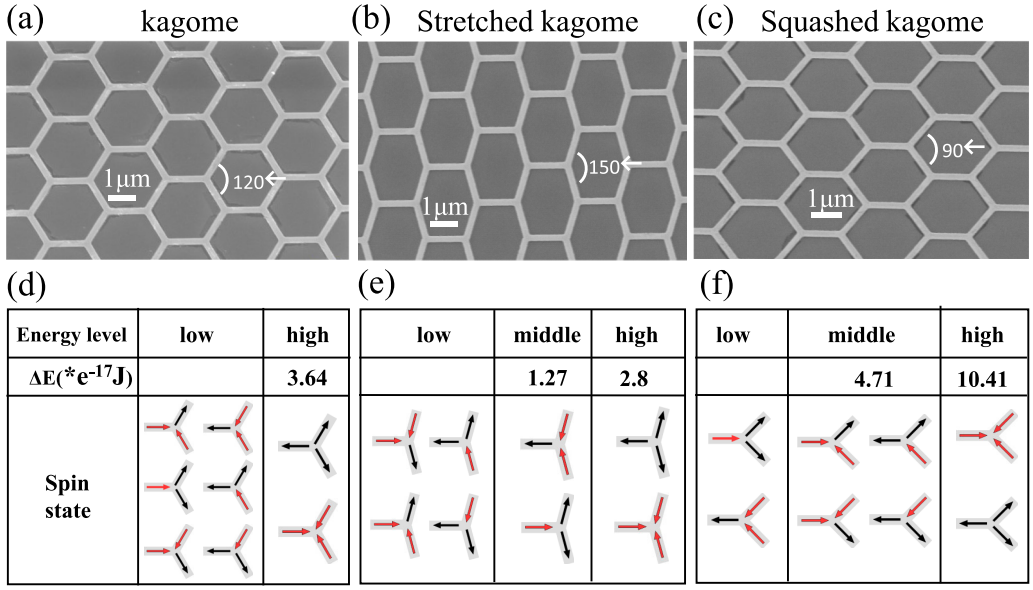

FIG. 1. (a)–(c) SEM images of artificial kagome spin ice structures: (a) standard kagome, (b) stretched kagome, and (c) squashed kagome. The three branches are labeled as α, β, and γ, respectively. (d),(e) The energy differences of each spin state respective to the lowest energy state of each kagome spin ice. The red or black arrows indicate the spins pointing into or out from the vertices.

spin ices strongly depend on the initial state of magnetization within the third bar. The energy landscape of the deformed kagome ice becomes multileveled, allowing for the induction of various reversal behaviors by selectively adjusting the initial state to different energy levels. Our results suggest that the characteristics of these reversal behaviors can be manipulated not only by changing the deformation of the system but also by adjusting the initial state.

II. EXPERIMENT AND SIMULATION METHOD

Our study focused on two types of deformed kagome patterns: stretched kagome and squashed kagome. We achieved these patterns by applying compression along the horizontal and vertical directions, respectively, as depicted in scanning electron microscope (SEM) images in Figs. 1(b) and 1(c). To provide a basis for comparison, we also fabricated standard kagome ice patterns, shown in the SEM image in Fig. 1(a). The islands' dimensions were 180 nm × 1100 nm with a thickness of 20 nm. We fabricated the Permalloy ($Fe_{20}Ni_{80}$) islands using *e*-beam lithography on a silicon substrate, followed by electron beam evaporation and lift-off processes. It is important to note that all structures in this study were designed with open edges. We denoted the sublattice bars in the horizontal direction as α, while the upward and downward bars were denoted as β and γ, respectively. The angle between the β and γ bars was chosen to be 150° for the stretched kagome and 90° for the squashed kagome patterns.

The acquired domain images were captured using a commercial Magneto-Optical Kerr Effect (MOKE) microscope manufactured by Evico Magnetics GmbH. To visualize the magnetic state in each sub-200 nm wide bar, a 100× oil lens with a numerical aperture of 1.3 was employed for high-resolution domain imaging. A white-color light-emitting diode with a broad wavelength range (420–650 nm) served as the light source in this study. Kerr signals were measured in the longitudinal geometry, with light incident in two optical planes orthogonal to each other; thus this setup allows for the simultaneous imaging of both M_x and M_y components during a magnetic field sweep without altering the imaging conditions [28,31].

To enhance magnetic domain contrast, we subtracted an image with domain information at a certain state from a background image captured right before the reversal occurs. This subtraction results in a differential image that eliminates topographic information. The IMAGEJ software's drifting-correction function was further employed to mitigate time-dependent drifting effects. However, it is important to note that only drifting effects over very short durations could be effectively corrected. Consequently, we can only display magnetic domain images at the early stages of the reversal process.

The energy landscape of the deformed structures was calculated through micromagnetic simulation using MUMAX3 [32] on a single vertex in the three spin ice structures shown in Figs. 1(d)–1(f). In the simulation, each bar in the vertex has a size of 1100 × 180 × 20 nm^3, same as the bar size in experiments. We used a mesh size of 5 × 5 × 20 nm^3 and typical material parameters of permalloy (Py), such as an exchange constant of 1.3 × 10^{11} J m^{-1}, saturation magnetization of 800 kA m^{-1}, and Gilbert damping of 0.01. Both exchange and dipolar interactions were considered in our simulations.

III. RESULTS AND DISCUSSION

The energy landscapes of standard and deformed kagome spin ices are calculated through micromagnetic simulations, and the results are illustrated in Figs. 1(d)–1(f).

For the connected kagome spin ice, the dominant exchange interaction leads to the emergence of the ice rule. This rule

dictates the configurations such as 2-in-1-out or 1-in-2-out in the low-energy regime with highly degenerate spin states due to the threefold symmetry of the structure. As depicted in Fig. 1(d), the configurations with "3-in" or "3-out" possess higher energy. However, the introduction of asymmetry partially lifts the degeneracy and alters the energy hierarchy. As illustrated in Figs. 1(e) and 1(f), the low-energy configurations split into two energy levels. In the stretched kagome spin ice, the β and γ bars exhibit a "head to tail" alignment in the lowest energy state while still adhering to the "2-in-1-out" or "1-in-2-out" alignment in the vertex spin configuration. Conversely, in squashed kagome ice, the β and γ bars at the ground state prefer a "head-to-head" alignment while following the same vertex spin configuration rules. The energy difference of each energy level with respect to the lowest energy state in each structure is also provided in Figs. 1(e) and 1(f). Notably, the energy difference in squashed kagome ice is significantly higher than in the other structures, primarily due to the smaller angle between the β bar and γ bar. This discrepancy in energy difference makes the transition between the two energy states in squashed kagome ice challenging during the reversal process. The presence of multilevel energy states, along with adherence to the ice rule in deformed kagome ice, contributes to the emergence of diverse magnetization reversal behavior.

We initiated our study by measuring the hysteresis loops at various field angles θ_H. Figures 2(a)–2(f) display the representative hysteresis loops of stretched and squashed kagome spin ices obtained at different θ_H. The definitions of the x and y directions, as well as the angle θ_H, are provided in the inset of each respective panel. Our measurements revealed that the hysteresis loops of both the M_x and M_y components are sensitive to θ_H. Specifically, for $\theta_H = 0°$, both structures exhibit zero M_y during the field sweeping process. In the stretched kagome structure, M_x gradually reverses [Fig. 2(a)], while in the squashed kagome structure [Fig. 2(d)], M_x displays a sharp switch. When the field aligns nearly perpendicular to the γ bars of the system ($\theta_H = 15°$ for stretched kagome and $\theta_H = 40°$ for squashed kagome), the hysteresis loops from both structures in Figs. 2(b) and 2(e) display a two-step magnetization switch, and the two switching fields are denoted as H_{c1} and H_{c2}, respectively. As the field approaches the vertical direction, the hysteresis loops of both M_x and M_y in these two structures exhibit a single-step loop. To systematically describe the hysteresis loop response to θ_H, we quantified H_{c1} and H_{c2} for these structures by varying θ_H from $-90°$ to $90°$ with a $5°$ step. The results for standard kagome, stretched kagome, and squashed kagome structures are presented in Figs. 3(a)–3(c), respectively.

As depicted in Fig. 3(a), H_{c1} in standard kagome structure remains nearly angular independent, primarily due to the influence of the ice rule [28]. In contrast, in the case of the deformed kagome structures, H_{c1} exhibits two jumps at field angles where the applied field angle aligns perpendicular to the γ or β bars. For the stretched kagome, these H_{c1} jumps occur at $\theta_H = 15°$ and $-15°$, while for the squashed kagome, they occur at $\theta_H = 45°$ and $-45°$, as illustrated in Figs. 3(b) and 3(c). The reason for this discrepancy lies in the alteration of the initial state of the system as the applied field crosses the critical field angle. Specifically, when $\theta_H > 15°$ and $\theta_H < 15°$,

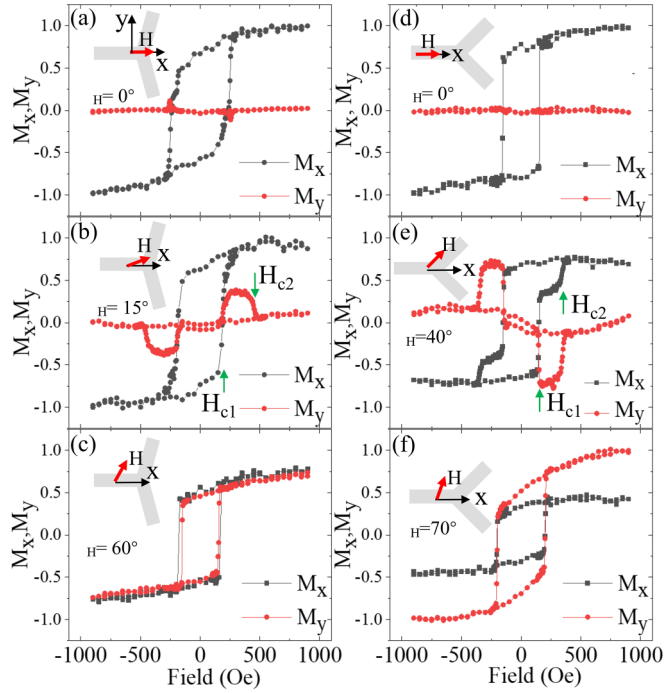

FIG. 2. The typical hysteresis loops of M_x and M_y components measured from (a)–(c) stretched and (d),(e) squashed kagome spin ices with different field angle θ_H. (a)–(c) The loops of the stretched kagome spin ice with θ_H equal to (a) 0°, (b) 15°, and (c) 60°. (d)–(f) The loops of the squashed kagome spin ice with θ_H equal to (d) 0°, (e) 40°, and (f) 70°. The inset in each figure sketches the field direction with respect to the pattern geometry. The red M_x loop in each figure is normalized by the saturation Kerr signal of M_x with $\theta_H = 0°$, and the black M_y loop is normalized by the saturation Kerr signal of M_y with $\theta_H = 90°$. The green arrows in (b),(c) indicate the field H_{c1} and H_{c2}.

the initial states of the stretched kagome reside in different energy levels. Consequently, this leads to avalanche behaviors taking place at distinct field strengths. This inference is substantiated by real-space magnetic domain images, as elaborated upon in the subsequent text.

In contrast, H_{c2} exhibits strong field angular dependence in all three structures. This dependence arises because H_{c2} represents the reversal field required for the remaining unflipped bars after the avalanches have occurred. The field angular dependence in H_{c2} stems from the fact that magnetization reversal in a single bar can be described by the curling model which exhibits angular dependence [33–36].

Consequently, the peaks of H_{c2} occur at angles where the applied field is perpendicular to the β or γ bars. It is unsurprising that for standard kagome spin ice, the peaks of H_{c2} arise at $\theta_H = 60°$ and $-60°$. Similarly, for the stretched kagome, the peaks of H_{c2} arise at $\theta_H = 15°$ and $-15°$, and for the squashed kagome, the peaks of H_{c2} arise at $\theta_H = 45°$ and $-45°$, as illustrated in Figs. 3(a)–3(c).

Furthermore, when $\theta_H = 0°$, the magnetization reversal in these three different structures shows distinct features. In standard kagome, a single-step magnetization reversal occurs within a narrow field angle range from $\theta_H = -7°$ to $7°$. However, for stretched kagome, this single-step magnetization

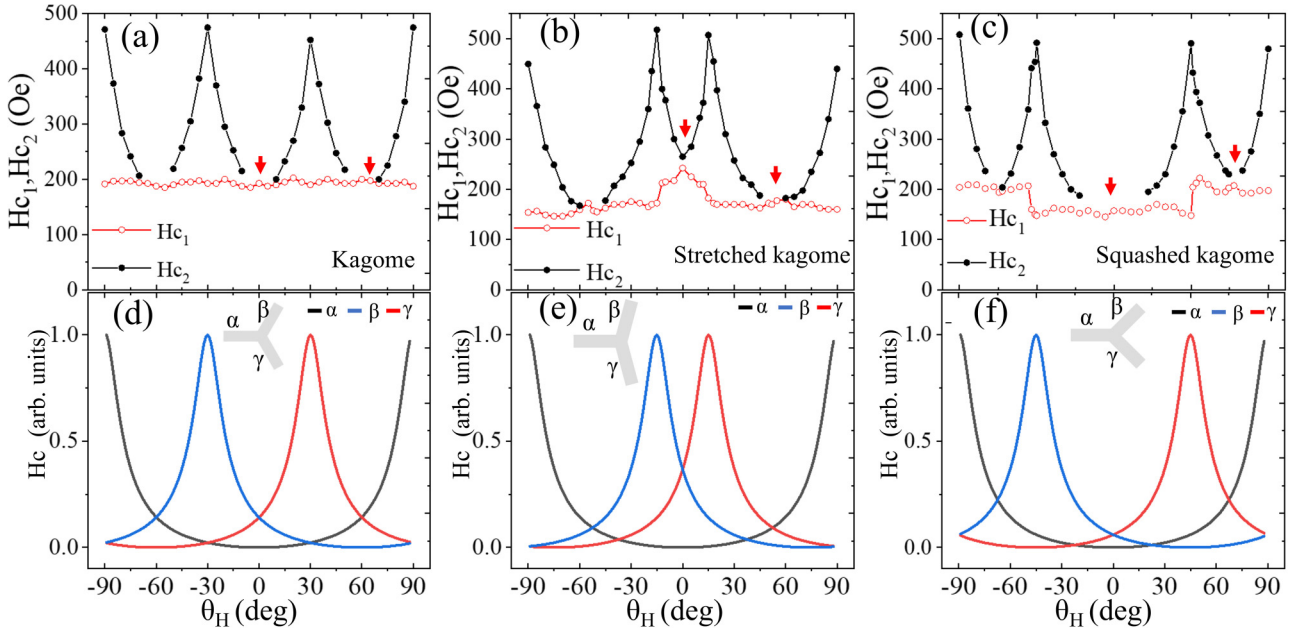

FIG. 3. (a)–(c) The θ_H dependence of reversal fields H_{c1} and H_{c2} for (a) kagome, (b) stretched kagome, and (c) squashed kagome. (d)–(f) The calculated reversal field of each individual bar based on the curling model as a function of θ_H for (d) kagome, (e) stretched kagome, and (f) squashed kagome. The red arrows in (a)–(c) indicate the field angles where the simulation does not agree with the experimental results.

reversal is absent. In contrast, for squashed kagome, a single-step magnetization reversal occurs within a wide field angle range of $\theta_H = -20^\circ$ to 20°. To gain a deeper understanding of the distinction features in the deformed kagome structures, we performed numerical calculation of the curves using the curling model [33–36]. The magnetization reversal in an infinite cylinder proceeds via spin curling rather than uniform rotation, which is called the curling mode [35]. Due to the high aspect ratio of the nanowire in the kagome ice network, the angular-dependent coercive field in the kagome ice network can be well described by the curling model [25,28]. In the curling model, the reversal field can be described as $H_c \propto \frac{a(1+a)}{\sqrt{a^2+(1+2a)\cos^2\theta}}$ where $a = 1.08(2\lambda_{ex}/s)^2$. Here, λ_{ex} represents the exchange length, s represents the cross-sectional length of each bar ($s = \sqrt{tw}$ with t and w as the thickness and width of each bar), and θ is the field angle respective to the bar direction.

To investigate the angular dependence of the coercive field within the kagome network, we plotted the coercive fields of three individual bars with different angles, as illustrated in Figs. 3(b)–3(f). Compared to the experimental data, the curling model accurately fits the variation of H_{c2}, confirming that this variation of H_{c2} originates from the magnetization reversal in individual bars. However, it falls short in explaining the occurrence of the single-step magnetization reversal. The variation of H_{c1} cannot be simply explained based on the curling model. To gain a deeper understanding of this phenomenon, we employed an imaging approach to observe the avalanche behaviors occurring at different field angles within the deformed kagome structures. The imaging process commenced by initializing the system with a saturated field applied in the opposite direction ($\theta_H - 180^\circ$) and then gradually decreasing and reversing the field. The states before the reversal serve as the reference states, and subsequent reversal behaviors were imaged throughout the field sweeping process.

For each selected angle, both the M_x and M_y components were taken to acquire complementary information about the magnetization reversal behavior. In the case of the stretched kagome structure, at $\theta_H = 0^\circ$, as illustrated in Figs. 4(a) and 4(b), the stochastically magnetization reversal is present. Due to the sensitivity of the M_x and M_y measurements, the reversal of the α bars is visible in the M_x images, while the reversals of the β and γ bars are visible in the M_y images. The insets in Figs. 4(a) and 4(b) highlighted by the green rectangles demonstrate the armchairlike reversal chain, which consists of two types of low-energy states sketched in Fig. 4(a). The magnetization reversal within these chains occurs either by reversing the magnetization of the α bars followed by the β bars or by collectively reversing the magnetization of the α bars followed by the γ bars, as illustrated in the inset. We refer to these two distinct reversal paths as the $\alpha+\beta$ chain or the $\alpha+\gamma$ chain, respectively. These behaviors starkly contrast with those observed in the standard kagome structure, where avalanches can span the entire system [28].

These observed behaviors align with the principles of the ice rule. When the stretched kagome spin ice is saturated along the $-\theta_H$ direction, the system is in a middle-energy state, as depicted in the inset of Fig. 4(a). During the field reversal process, the α bars are the first to reach their nucleation field due to their stronger Zeeman energy compared to the other bars. However, reversing the α bars alone would lead to an unfavorable energy state at the vertices. Instead, the more favorable choice is to reverse the magnetization of either the $\alpha+\beta$ chain or the $\alpha+\gamma$ chain. Consequently, the actual reversal event does not occur until the applied field

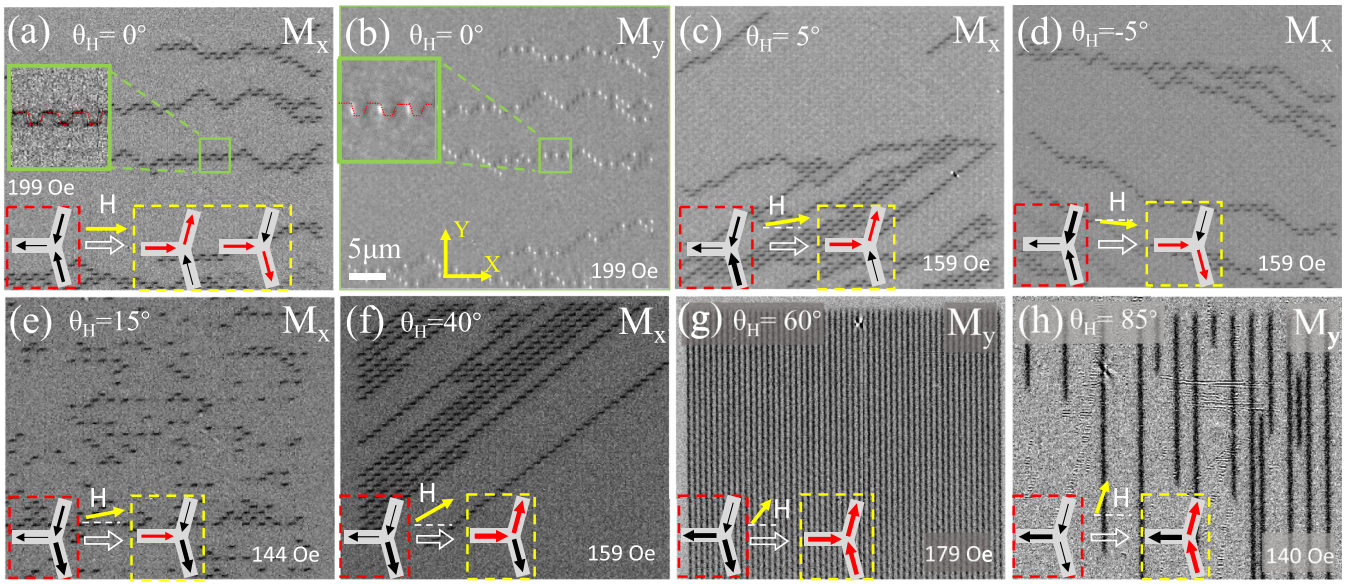

FIG. 4. The real-space magnetization images of the stretched kagome structure with either M_x or M_y components during the magnetization reversal process at various θ_H angles: (a) M_x at $\theta_H = 0°$, (b) M_y at $\theta_H = 0°$, (c) M_x at $\theta_H = 5°$, (d) M_x at $\theta_H = -5°$, (e) M_x at $\theta_H = 15°$, (f) M_x at $\theta_H = 40°$, (g) M_y at $\theta_H = 60°$, and (h) M_y at $\theta_H = 85°$. The inset in the red square in each image provides the sketched initial spin orientation in each bar, and the width of the arrow for each bar indicates the relative strength of the reversal field required to induce the magnetization reversal of the sublattice. The actual reversed spin configurations are depicted in the yellow squares, where red bars represent the flipped spins. The insets in (a,b) show the magnified images with the armchairlike switching chains extracted from the regions highlighted by the green rectangles. A coordinate system which defines the x and y directions is illustrated in (b).

reaches a critical value capable of reversing the β or γ bars. Specifically, in the stretched kagome structure, magnetization reversal transpires through stochastic processes involving either the $\alpha+\beta$ chain or the $\alpha+\gamma$ chain with equal probability, as both choices are energetically degenerate. This stochastic nature of reversal leads to the formation of armchairlike chains during the reversal process. When the external field slightly tilts, the Zeeman energy favors the reversal of either the β bars or the γ bars, resulting in a decrease in the energy required to trigger an avalanche (H_{c1} decreases). Conversely, the remaining unreversed bars (α bars) require more energy to reverse, leading to an increase in H_{c2}. Consequently, the reversal path tends to proceed via the $\alpha+\beta$ chain when $\theta_H = 5°$, as shown in Fig. 4(c), and via the $\alpha+\gamma$ chain when $\theta_H = -5°$, as shown in Fig. 4(d). Notably, the avalanche behavior undergoes a significant change when the angle θ_H reaches 15°. Specifically, when θ_H exceeds 15° ($\theta_H > 15°$), the initial state of the γ bars differs from the case when θ_H is less than 15° ($\theta_H < 15°$). As a result, reversing the α bar no longer violates the ice rule, leading to a significant decrease in H_{c1} when the field angle exceeds 15°. This is because the energy required to reverse a single bar is lower than that needed to trigger a chain of bars. This feature aligns with the H_{c1} measurement results of the stretched kagome shown in Fig. 3(b). In this scenario, all the α bars reverse first, as depicted in the inset of Fig. 4(e). Subsequently, the β bars and γ bars undergo separate reversals due to the substantial difference in their reversal fields. Consequently, no collective reversal behavior occurs throughout the process. For $\theta_H > 37.5°$, the system once again exhibits collective reversal behaviors. This resurgence can be attributed to the coercive field (H_c) of the β bars becoming lower than that of the α bars at this specific angle. Reversing the β bars alone would violate the ice rule. Consequently, the $\alpha+\beta$ chain undergoes collective magnetization reversal, forming a linear avalanche pattern as depicted in Fig. 4(f). Note that the linear avalanche always chains together in this reversal process. This is because the magnetization reversal of the $\alpha+\beta$ chain leads the system into a middle-energy state and, therefore, the reversal process always involves the magnetization reversal of the γ bars contributing to a decrease in system energy. This trend becomes more obvious as θ_H increases, with the reversal field of the γ bar continuously decreasing. As a result, the reversal behavior in the two-step reversal process in Fig. 2(b) becomes less separated. The bars in three sublattices tend to reverse collectively, eventually encompassing the entire system when θ_H is approximately 60°, as illustrated in Fig. 4(g). When θ_H is close to the vertical direction, a linear avalanche arises, as shown in Fig. 4(h). This phenomenon has a mechanism similar to the one that occurred at $\theta_H = 40°$. The difference is that the linear avalanche does not tend to chain together in this case, as the magnetization reversal of the α bar does not help the system reach a low-energy state. As described above, the observed avalanche behaviors are strongly associated to the ice rule.

In squashed kagome spin ice, the initial state of the system is set to a low-energy configuration around $\theta_H = 0°$ by a negative field, as illustrated in the inset of Fig. 5(a). When applying a positive field, the entire spin configuration rapidly transforms into the other degenerate low-energy state without the occurrence of intermediate states. A reversal defect can be found in the blue dashed square in Fig. 5(a), indicating the area consisting of unreversed bars. This can be attributed to

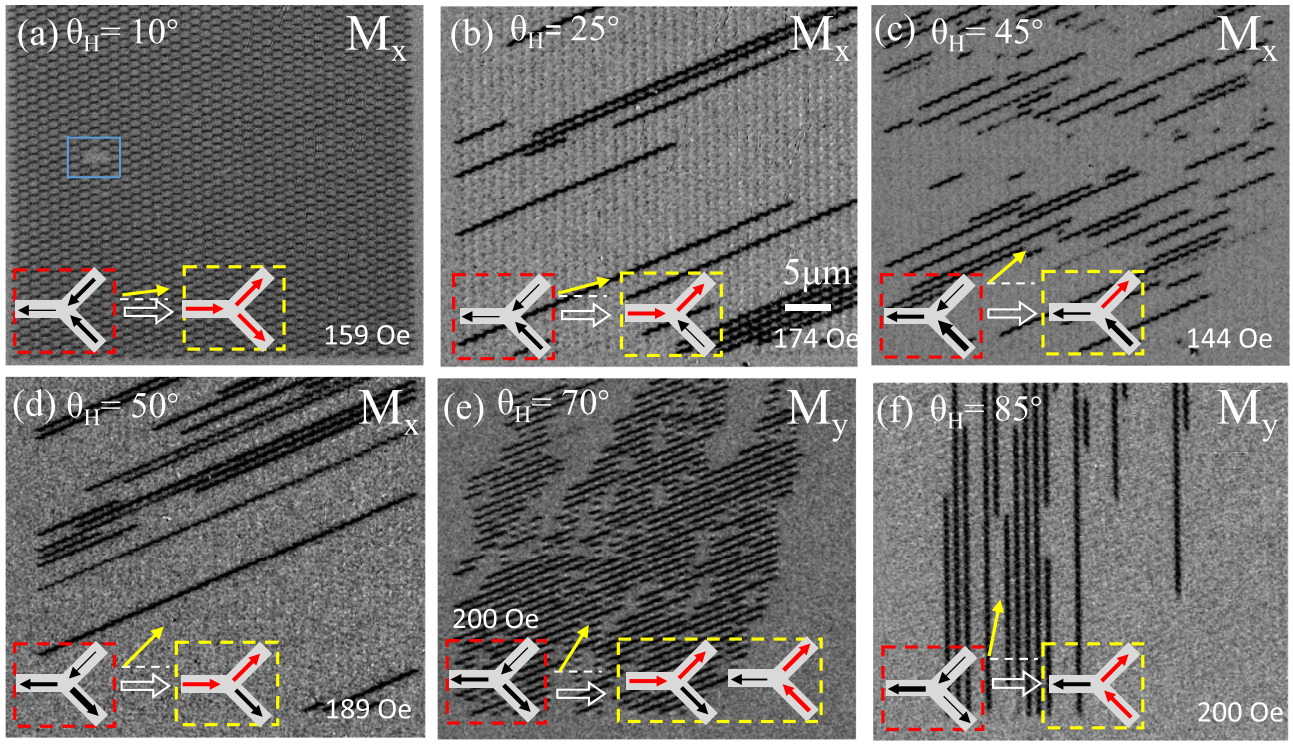

FIG. 5. Selected sequential Kerr microscopy images of the squashed kagome spin ice with either M_x or M_y components during the magnetization reversal process at different θ_H angles: (a) $\theta_H = 10°$, (b) $\theta_H = 25°$, (c) $\theta_H = 45°$, (d) $\theta_H = 50°$, (e) $\theta_H = 70°$, and (f) $\theta_H = 85°$. The initial spin states are depicted in the inset within the red squares, with arrow width indicating distinct levels of the reversal field strength required to induce the reversal of the sublattice. The actual reversed spin configurations are sketched in the yellow squares, where red arrows indicate the flipped spins. The scale bar is shown in (b).

the local defect where certain bars possess a higher reversal field. As a result, local neighboring bars experience hindered reversal due to the ice rule. This avalanche-type switch exhibits similarities to the switch behavior observed in standard kagome structure [28]. However, in squashed kagome structure, this avalanche-type reversal process persists for θ_H up to 20°, but the same avalanche reversal in standard kagome only happens for θ_H less than 5° [28]. This difference can be attributed to the significant energy gap between the middle energy level and the ground energy level in the squashed kagome structure, which is considerably larger than in the standard kagome structure (see Fig. 1).

For $\theta_H >$ 20°, the avalanche-type reversal phenomenon disappears, and the magnetization reversals occur through the α+β chains, resulting in a stringlike avalanche behavior, as depicted in Fig. 5(b). In this scenario, the significant discrepancy in the reversal fields between the β bars and the γ bars, as shown in Fig. 3(f), is sufficient to break the constraint of the ice rule, leading to a two-step reversal process. As shown in Fig. 3(f), with increasing θ_H, the switch field becomes smaller for the β bar, but shows the opposite trend for the α bar. Consequently, it becomes harder to switch the magnetization in the α bars, but easier for the magnetization reversal in the β bars. Thus, in the stringlike avalanche behavior for $\theta_H >$ 20°, many shorter strings can appear, as shown in Fig. 5(c) with $\theta_H \sim 45°$.

However, the situation becomes different for $\theta_H > 45°$. In this situation, the β bars exhibit the lowest switching field. It is important to note that the initial magnetization in the γ bars points into the vertex. Therefore, if the magnetization in the β bars switches first, it would lead to a "3-in" configuration that violates the ice rule. Consequently, the α+β chain configuration reappears, driving the system back into a low-energy state. This transition from single switching in the β bar to collective switching in the α+β chain when θ_H exceeds 45° causes a significant jump in H_{c1}, as shown in Fig. 3(f). As θ_H further increases, the switching field for the α bar increases with θ_H, while H_c for the γ bar keeps decreasing. As shown in Fig. 3(f), the H_c's for the α bar and γ bar exhibit a crossing behavior at $\theta_H = 72.5°$. Then, for $\theta_H > 75°$, the stringlike switching behavior happens along the β+γ chains [Fig. 5(f)]. At $\theta_H \sim 72.5°$, the reversal process can occur via either the α+β chain or the β+γ chain [Fig. 5(e)], resulting in a single-step switching. Therefore, the magnetization reversal in squashed kagome structures can be well understood through considerations of system energy and adherence to the ice rule.

As shown in Fig. 3, when the applied field is perpendicular to the γ bar ($\theta_H = 15°$ for the stretched structure, and $\theta_H = 45°$ for the squashed structure), the switch field H_{c1} exhibits a noticeable jump. This unique behavior is reflected in the magnetization reversal patterns seen in Figs. 4 and 5 under these specific conditions. This behavior may be associated with the fact that the initial magnetization in the γ bars can switch direction, suggesting that the magnetization reversal in a deformed kagome structure depends on the initial state of the

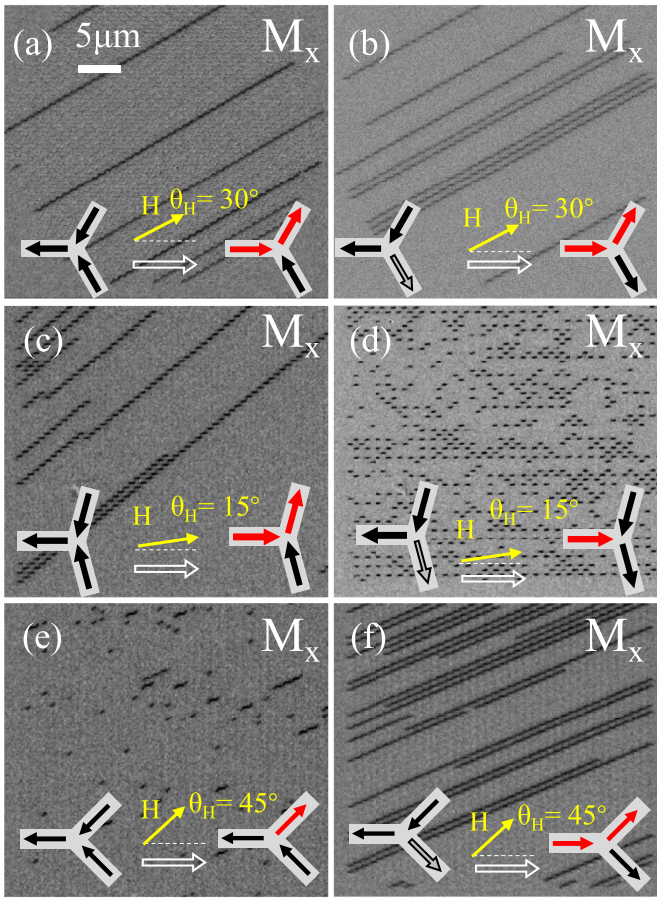

FIG. 6. Different reversal behaviors induced by varying the magnetization orientation in the γ bar: (a),(b) standard kagome, (c),(d) stretched kagome, and (e),(f) squashed kagome. The insets in each figure show the initial state and the reversed state, with red arrows indicating the flipped spins and black arrows indicating the unflipped spins. The field was applied perpendicular to the γ bar in each measurement as indicated by the yellow arrow in each figure. The scale bar is shown in (a).

system. In contrast, the H_{c1} for the standard kagome structure shows constant angular dependence [Fig. 3(a)], indicating no effect of the different magnetization orientations of the γ bars.

In our experimental setup, by applying a magnetic field along a certain direction, we could initially configure the system such that the magnetization pointed out from the vertex in the α bars and into the vertex in the β bars, as illustrated in the inset of Fig. 6. However, the magnetization in the γ bars could be set either pointing into or out of the vertex. In order to prepare the initial state with the magnetization in the γ bars pointing into the vertex, we first applied a 1000 Oe field with $\theta_H = 180°$, and then gradually reduced the field to zero. For the initial state with the magnetization in the γ bars pointing out of the vertex, we applied a 1000 Oe field with $\theta_H = -100°$, and then gradually reduced the field to zero. The different initial states result in a large difference in the coercive field for each sublattice.

The reversal behaviors for different initial states for standard kagome are imaged and illustrated in Figs. 6(a) and 6(b). The results reveal that the one-dimensional (1D) stringlike avalanche behavior remains consistent regardless of the initial magnetization orientation in the γ bar. However, in the stretched kagome structure, as shown in Figs. 6(c) and 6(d), the switching behavior at H_{c1} exhibits a distinct difference depending on the initial magnetization orientation in the γ bar.

However, within the stretched kagome structure, as depicted in Figs. 6(c) and 6(d), we observed a notable difference in the switching behavior at H_{c1} based on the initial magnetization orientation in the γ bar. When the magnetization in the γ bar points into the vertex [Fig. 6(c)], a 1D stringlike avalanche along the $\alpha+\beta$ chain is observed. Conversely, when the magnetization in the γ bar points out from the vertex [Fig. 6(d)], discrete magnetization reversal behavior occurs in the α bar. In the squashed kagome structure, as shown in Figs. 6(e) and 6(f), a 1D stringlike avalanche along the $\alpha+\beta$ chain is observed when the magnetization in the γ bar points out from the vertex [Fig. 6(e)], while discrete magnetization reversal behavior appears in the β bar when the magnetization in the γ bar points into the vertex [Fig. 6(f)]. Such discrete magnetization reversal behavior clearly demonstrates the effect of the degeneracy break in the deformed kagome structure due to the structural deformation, since this discrete reversal behavior has been rarely observed in kagome spin ice structures with the sixfold degeneracy of the ground state. Our results also highlight that the manipulation of the initial state of the deformed kagome system can selectively control the reversal behaviors.

IV. CONCLUSION

In summary, we employed high-resolution Kerr microscopy to investigate the magnetization reversal behavior in deformed kagome spin ice structures. The introduction of deformation breaks the structural symmetry and alters the energy hierarchy of the system, leading to emerging phenomena due to the ice rule. Compared with the standard kagome spin ice, deformed kagome spin ices exhibit unique avalanche behaviors, including armchairlike avalanches and discretelike reversal behaviors. Besides, the energy landscape in deformed kagome ice become multilevel, which enables the manipulation of the initial states of the system. Selectively adjusting the initial states can control the pathway of magnetization reversal behaviors. These findings enhance the tunability of the artificial spin ice system's response to external magnetic fields, holding significant implications for high-density memory storage applications.

ACKNOWLEDGMENTS

The work was supported by the National Key Research and Development Program of China (Grant No. 2022YFA1403300), the National Natural Science Foundation of China (Grants No. 11974079, No. 12274083, and No. 12221004), the Shanghai Municipal Science and Technology Major Project (Grant No. 2019SHZDZX01), and the Shanghai Municipal Science and Technology Basic Research Project (Grants No. 22JC1400200 and No. 23dz2260100).

[1] R. F. Wang, C. Nisoli, R. S. Freitas, J. Li, W. McConville, B. J. Cooley, M. S. Lund, N. Samarth, C. Leighton, V. H. Crespi, and P. Schiffer, Artificial 'spin ice' in a geometrically frustrated lattice of nanoscale ferromagnetic islands, Nature (London) **439**, 303 (2006).

[2] Y. Qi, T. Brintlinger, and J. Cumings, Direct observation of the ice rule in an artificial kagome spin ice, Phys. Rev. B **77**, 094418 (2008).

[3] J. P. Morgan, A. Stein, S. Langridge, and C. H. Marrows, Thermal ground-state ordering and elementary excitations in artificial magnetic square ice, Nat. Phys. **7**, 75 (2010).

[4] J. Li, X. Ke, S. Zhang, D. Garand, C. Nisoli, P. Lammert, V. H. Crespi, and P. Schiffer, Comparing artificial frustrated magnets by tuning the symmetry of nanoscale permalloy arrays, Phys. Rev. B **81**, 092406 (2010).

[5] Z. Budrikis, J. P. Morgan, J. Akerman, A. Stein, P. Politi, S. Langridge, C. H. Marrows, and R. L. Stamps, Disorder strength and field-driven ground state domain formation in artificial spin ice: Experiment, simulation, and theory, Phys. Rev. Lett. **109**, 037203 (2012).

[6] C. Nisoli, R. Moessner, and P. Schiffer, Artificial spin ice: Designing and imaging magnetic frustration, Rev. Mod. Phys. **85**, 1473 (2013).

[7] V. S. Bhat, J. Sklenar, B. Farmer, J. Woods, J. T. Hastings, S. J. Lee, J. B. Ketterson, and L. E. DeLong, Controlled magnetic reversal in Permalloy films patterned into artificial quasicrystals, Phys. Rev. Lett. **111**, 077201 (2013).

[8] I. Gilbert, G. W. Chern, S. Zhang, L. O'Brien, B. Fore, C. Nisoli, and P. Schiffer, Emergent ice rule and magnetic charge screening from vertex frustration in artificial spin ice, Nat. Phys. **10**, 670 (2014).

[9] Y. Perrin, B. Canals, and N. Rougemaille, Extensive degeneracy, Coulomb phase and magnetic monopoles in artificial square ice, Nature (London). **540**, 410 (2016).

[10] Y. L. Wang, Z. L. Xiao, A. Snezhko, J. Xu, L. E. Ocola, R. Divan, J. E. Pearson, G. W. Crabtree, and W. K. Kwok, Rewritable artificial magnetic charge ice, Science **352**, 962 (2016).

[11] D. Shi, Z. Budrikis, A. Stein, S. A. Morley, P. D. Olmsted, G. Burnell, and C. H. Marrows, Frustration and thermalisation in an artificial magnetic quasicrystal, Nat. Phys. **14**, 309 (2018).

[12] V. Schánilec, B. Canals, V. Uhlíř, L. Flajšman, J. Sadílek, T. Šikola, and N. Rougemaille, Bypassing dynamical freezing in artificial kagome ice, Phys. Rev. Lett. **125**, 057203 (2020).

[13] W. C. Yue, Z. Yuan, Y. Y. Lyu, S. Dong, J. Zhou, Z. L. Xiao, L. He, X. Tu, Y. Dong, H. Wang, W. Xu, L. Kang, P. Wu, C. Nisoli, W. K. Kwok, and Y. L. Wang, Crystallizing kagome artificial spin ice, Phys. Rev. Lett. **129**, 057202 (2022).

[14] K. Hofhuis, S. H. Skjærvø, S. Parchenko, H. Arava, Z. C. Luo, A. Kleibert, P. M. Derlet, and L. J. Heyderman, Real-space imaging of phase transitions in bridged artificial kagome spin ice, Nat. Phys. **18**, 699 (2022).

[15] C. Castelnovo, R. Moessner, and S. L. Sondhi, Magnetic monopoles in spin ice, Nature (London) **451**, 42 (2008).

[16] A. Pushp, T. Phung, C. Rettner, B. P. Hughes, S. H. Yang, L. Thomas, and S. S. P. Parkin, Domain wall trajectory determined by its fractional topological edge defects, Nat. Phys. **9**, 505 (2013).

[17] S. Ladak, D. E. Read, G. K. Perkins, L. F. Cohen, and W. R. Branford, Direct observation of magnetic monopole defects in an artificial spin-ice system, Nat. Phys. **6**, 359 (2010).

[18] G. Chern, C. Reichhardt, and C. J. O. Reichhardt, Avalanches and disorder-induced criticality in artificial spin ices, New J. Phys. **16**, 063051 (2014).

[19] S. A. Daunheimer, O. Petrova, O. Tchernyshyov, and J. Cumings, Reducing disorder in artificial kagome ice, Phys. Rev. Lett. **107**, 167201 (2011).

[20] P. Mellado, O. Petrova, Y. C. Shen, and O. Tchernyshyov, Dynamics of magnetic charges in artificial spin ice, Phys. Rev. Lett. **105**, 187206 (2010).

[21] Y. C. Shen, O. Petrova, P. Mellado, S. Daunheimer, J. Cumings, and O. Tchernyshyov, Dynamics of artificial spin ice: A continuous honeycomb network, New J. Phys. **14**, 035022 (2012).

[22] K. Zeissler, S. K. Walton, S. Ladak, D. E. Read, T. Tyliszczak, L. F. Cohen, and W. R. Branford, The non-random walk of chiral magnetic charge carriers in artificial spin ice, Sci. Rep. **3**, 1252 (2013).

[23] J. Drisko, S. Daunheimer, and J. Cumings, $FePd_3$ as a material for studying thermally active artificial spin ice systems, Phys. Rev. B **91**, 224406 (2015).

[24] S. Ladak, D. E. Read, W. R. Branford, and L. F. Cohen, Direct observation and control of magnetic monopole defects in an artificial spin-ice material, New J. Phys. **13**, 063032 (2011).

[25] D. M. Burn, M. Chadha, and W. R. Branford, Angular-dependent magnetization reversal processes in artificial spin ice, Phys. Rev. B **92**, 214425 (2015).

[26] S. K. Walton, K. Zeissler, D. M. Burn, S. Ladak, D. E. Read, T. Tyliszczak, L. F. Cohen, and W. R. Branford, Limitations in artificial spin ice path selectivity: The challenges beyond topological control, New J. Phys. **17**, 013054 (2015).

[27] M. Tanaka, E. Saitoh, H. Miyajima, T. Yamaoka, and Y. Iye, Magnetic interactions in a ferromagnetic honeycomb nanoscale network, Phys. Rev. B **73**, 052411 (2006).

[28] D. Shi, H. Chen, J. Xu, H. Xia, Y. Chen, and Y. Wu, Kerr microscopy real-time imaging of the magnetization reversal process in kagome artificial spin ice, Phys. Rev. B **101**, 134428 (2020).

[29] P. A. M. Dirac, Quantised singularities in the electromagnetic field, Proc. R. Soc. A **133**, 60 (1931).

[30] L. D. C. Jaubert and P. C. W. Holdsworth, Signature of magnetic monopole and Dirac string dynamics in spin ice, Nat. Phys. **5**, 258 (2009).

[31] J. Xu, C. Zhou, M. Jia, D. Shi, C. Liu, H. Chen, G. Chen, G. Zhang, Y. Liang, J. Li, W. Zhang, and Y. Wu, Imaging antiferromagnetic domains in nickel oxide thin films by optical birefringence effect, Phys. Rev. B **100**, 134413 (2019).

[32] A. Vansteenkiste, J. Leliaert, M. Dvornik, M. Helsen, F. Garcia-Sanchez, and B. Van Waeyenberge, The design and verification of MuMax3, AIP Adv. **4**, 107133 (2014).

[33] E. C. Stoner and E. P. Wohlfarth, A mechanism of magnetic hysteresis in heterogeneous alloys, Philos. Trans. R. Soc., London **240**, 599 (1948).

[34] A. Aharoni and S. Shtrikman, Magnetization curve of the infinite cylinder, Phys. Rev. **109**, 1522 (1958).

[35] Y. Ishii, Magnetization curling in an infinite cylinder with a uniaxial magnetocrystalline anisotropy, J. Appl. Phys. **70**, 3765 (1991).

[36] W. Wernsdorfer, B. Doudin, D. Mailly, K. Hasselbach, A. Benoit, J. Meier, J.-Ph. Ansermet, and B. Barbara, Nucleation of magnetization reversal in individual nanosized nickel wires, Phys. Rev. Lett. **77**, 1873 (1996).